An Accurate and Robust Strip-Edge-Based Structured Light Means for Shiny Surface Micromeasurement in 3-D

Zhan Song, Ronald Chung, *Senior Member, IEEE*, and Xiao-Ting Zhang

***Abstract*—Three-dimensional measurement of shiny or reflective surface is a challenging issue for optical-based instrumentations. In this paper, we present a novel structured light approach for direct measurement of shiny target so as to skip the coating preprocedure. In comparison with traditional image-intensity-based structured light coding strategies like sinusoidal and line patterns, strip edges not raw image intensities are encoded in the illuminated patterns. With strip edges generally better preserved than individual image intensity in the image data in the presence of surface reflections, such a coding strategy is more robust. To remove the periodic ambiguity within strip patterns, traditional Gray code patterns are adopted. To localize the strip edges more precisely, both positive and negative strip patterns are used. An improved zero-crossing feature detector that has subpixel accuracy is proposed for strip-edge localization. The experimental setup is configured with merely an off-the-shelf pico-projector and a camera. Extensive experiments including accuracy evaluation, comparison with previous structured light algorithms, and the reconstruction of some real shiny objects are shown to demonstrate the system's accuracy and endurance against reflective nature of surfaces.**

***Index Terms*—Edge detection, shiny surface, structured light system (SLS), 3-D reconstruction.**

I. Introduction

WITH THE development of microfabrication and electronic packaging technology, there is in industry an increasing need of demanding three-dimensional (3-D) information in micrometer-level precision for surface inspection and quality control purposes [1], [2]. Even in mundane tasks like coin anticounterfeiting and signature recognition, it has been recognized that 3-D measurements that are necessarily at micrometer level constitute another level of enhancement to the existing 2-D methods. However, instruments and means for micrometer-level 3-D measurement in adequate accuracy and economy are still lacking. The fact that many of the target objects are shiny or reflective poses additional challenge to the measurement process.

By the working principles, 3-D measuring systems can be classified into coordinate measuring machines (CMMs), time of flight systems [3], stereo vision [4], shape from shading [5], laser scanning [6], and structured light systems (SLSs). Each approach comes with its own limitations, advantages, and cost. Compared with CMMs, optical-based methods have the advantages of being noncontact and fast and have been widely adopted in the commercial sector [7]. In these methods, laser beams or structured light patterns are projected onto the object surface, and the reflections are captured by imaging devices. Depth information at these illuminated areas can then be calculated via triangulation [8].

However, existing optical methods generally encounter difficulties with shiny or specular objects. Surfaces that are shiny generally have most of the incoming light beams reflected off the surfaces to various directions other than that of the imaging device, and that greatly compromises the quality of the captured images. Subject to the low image quality, existing structured light means which are usually intensity based [9]–[11] are difficult to operate. The often-used practice is to coat the shiny surfaces with a thin layer of white powder to have their reflective nature diminished. In particular, coating the surfaces with a thin opaque lacquer just for measuring purpose is a common practice. However, for applications where high accuracy is desired, such an additional coating film (usually with a thickness of 3–5 μm, which could be unevenly distributed over the surface) will induce distinct effect to the final measurement accuracy. More importantly, such a treatment complicates the whole scanning procedure and could cause corrosions to the target surface. All these make existing structured light scanning techniques impractical in many applications [12].

In this paper,a novel strip-edge based structured light coding strategy is presented. Information encoded in the pattern is not individual image intensity but strip-edge position. Compared with raw image intensities, strip edges have precise locations in the image data that are more distinguishable despite the presence of influence from the specular nature of the imaged scene to the overall image-intensity distribution. That makes its coding information more robust. To remove the periodic ambiguity with strip patterns, the traditional Gray code patterns

Manuscript received May 21, 2011; revised August 12, 2011, November 3, 2011, December 12, 2011, and January 11, 2012; accepted February 13, 2012. Date of publication February 24, 2012; date of current version October 16, 2012. This work was supported in part by the National Natural Science Foundation of China (NSFC) under Grant 61002040, in part by NSFC-GuangDong under Grant 10171782619-2000007, and in part by the Introduced Innovative R&D Team of Guangdong Province-Robot and Intelligent Information Technology Team.

Z. Song and X. T. Zhang are with the Shenzhen Institutes of Advanced Technology, Chinese Academy of Sciences, Shenzhen 518055, China (e-mail: zhan.song@siat.ac.cn; xt.zhang@siat.ac.cn).

R. Chung is with the Department of Mechanical and Automation Engineering, The Chinese University of Hong Kong, Shatin, Hong Kong (e-mail: rchung@mae.cuhk.edu.hk).

Color versions of one or more of the figures in this paper are available online at http://ieeexplore.ieee.org.

Digital Object Identifier 10.1109/TIE.2012.2188875

are adopted. By the use of both positive and negative strip patterns and a zero-crossing-based feature detector that we developed, strip edges can be extracted accurately. We show experimental results from a system setup that is configured with merely an off-the-shelf pico-projector and an industrial camera. Both devices are consumer grade to make the system economical and applicable for wide industrial applications.

This paper is organized as follows. Section II gives a brief review of the previous work on optical 3-D measuring technologies. The proposed structured light coding strategy, strip-edge detector, system calibration, and 3-D reconstruction are described in Section III. Experiments on accuracy evaluation, micrometer-level measurement of some real shiny objects, and comparisons with some traditional methods are presented in Section IV. A conclusion and possible future work are offered in Section V.

II. Previous Work

This work focuses on how high-accuracy 3-D measurement can be conducted over shiny micro-objects. Traditional mechanical probing means adopted in CMMs can achieve high precision, but at the expense of measuring speed [13]. Non-contact techniques, including laser scanning and SLS, have been advancing quickly in the last decade. Such techniques are triangulation-based optical measuring technologies. Laser scanner is operable on almost all surfaces, but because of its physical scanning-based nature, the operation speed is limited. The measuring accuracy is also affected by laser speckle effect [14]. SLSs consist of a projection device and cameras. By projecting some specially designed light patterns onto the target surface and imaging the illuminated scene, image points under the illuminations can each be labeled with a unique codeword. Such codewords are preserved in the image data. Since codewords on the projection side are known *a priori*, point-to-point correspondences between the image plane and the projection plane can be established readily. Three-dimensional information at such positions can then be determined via triangulation [8]. SLSs have the benefits of demanding only a simple setup, low cost, and fast operation speed, although its performance has certain dependence upon the surface condition of the inspected object and upon the working environment.

In the laser scanning approach, a beam of laser light is passed over the object while a camera mounted aside is to record the position of the projected laser profiles. There are an increasing number of off-the-shelf 3-D laser scanners available in the market. Differences of the various systems lie mainly on the laser strength, wavelength, working distance, and scanning speed. Representative systems in the market include Konica Minolta VIVID 9i and FARO Laser Scan Arm. There are also systems specifically for measuring in micrometer-level accuracy, like SICK IVP Ranger, which can achieve a resolution of $0.1 \times 0.5 \times 0.05$ mm in a measuring field of 150×25 mm. In [15], a 3-D laser scanning system is introduced for measuring wrinkles on laminated plastic sheets. The sensor uses single-spot laser illumination and performs position detection through subpixel peak detection. The laser displacement equipment is slightly tilted to minimize the effect of specular reflection from plastic surfaces. The sensor is set at a height of 30 mm above the plane of the mechanical stage and measures the distance to the target spot illuminated by the laser beam at a rate of 300 Hz. In the experiment, a depth resolution of 0.01 mm was reported. In [16], a laser line scanning system is studied. In the implementation, the camera and the laser are first calibrated. Having found the top and bottom boundaries of the laser line in the image, the center of the laser line between the top and bottom boundaries is found along its length. These center points are used for ray tracing and depth calculation. When measuring a weld pool of depth about 0.38 mm, a percentage error of about 9% was reported in the experiment. Instead of laser line, a light strip illuminated by a projection device can also be used with the same scanning strategy [17].

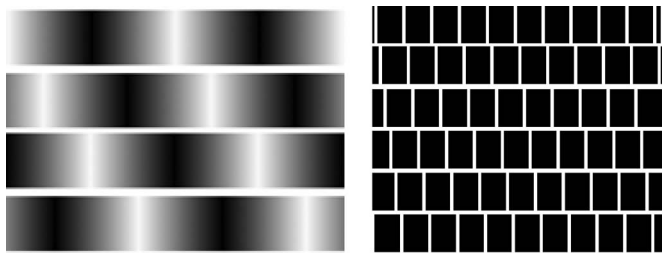

Fig. 1. (a) Sinusoidal pattern is shifted four times to let the phase value at each image point be determined [25]. (b) Line pattern is shifted six times to encode each image point on the line [27].

In the use of structured light pattern, the coding strategies can be categorized to spatial coding and temporal coding schemes [12], [18]. In the spatial coding scheme, codeword at a pattern element is defined by the pattern values in the neighborhood, which can be about various gray levels [19], colors [20], or some geometrical primitives [21] in the pattern. De-Bruijn sequences [22] and M-array [23] are the main coding schemes often employed. Since unique label at any pattern position comes with only a certain "spread" of pattern values in the vicinity of the position, the pattern positions that can be uniquely coded, and in turn their depth values subsequently recovered, cannot be too dense.

In the temporal coding scheme, coding is achieved not in the spatial domain but in the time domain. A series of patterns is projected at different instants onto the target surface. The codeword for any given pixel on the camera's image plane is decided by the illuminations at that pixel over time. SLSs using this encoding scheme can result in stronger data density and higher accuracy in the measurement. In particular, Gray code is a widely used coding scheme because of its simplicity and robustness. If a binary Gray code pattern of codeword length n is to be used, an image sequence consisting of $n + 1$ binary strip patterns need be projected sequentially to encode the scene. With that, the scene in the image domain can be separated into 2^n subregions, and the pixel center or the Gray code pattern's edges [24] are usually encoded.

To achieve higher measurement accuracy, methods like phase shifting [9]–[11], [25], [26] and line shifting [27] are usually used as shown in Fig. 1. To solve the periodic ambiguity between sinusoidal and line patterns, various phase unwrapping algorithms have been proposed [28], [29]. In real applications,

to improve the robustness of the unwrapping procedures, a series of Gray code patterns are usually used. By combining the local phase value and the global Gray code value, a unique codeword for each image point can be obtained. In experimenting with a sphere of 150-mm diameter, an average deviation of 0.05 mm was reported [25]. In [26], a sinusoidal shifting SLS is proposed for the 3-D measurement of flip chip solder bumps. In the measurement of a standard 1-mm gauge block, an average accuracy of 2 μm was obtained. However, subject to strong reflections of bump surfaces, the reconstructed 3-D models of the bumps have obvious discrepancy with the actual ones. In the line-shifting method [27], the sinusoidal periodic profile is substituted by a parallel line pattern as shown in Fig. 1(b). By consecutively shifting the line pattern six times in the x- and y-directions, respectively, six images for the x-coordinate and six images for the y-coordinate can be obtained. Since the line pattern is also periodic, it has inherent ambiguity, but the Gray code patterns can be brought in to remove the ambiguity. In an experiment that measures planarity, a standard deviation of 0.028 mm is reported in measuring a planar region of 200 $\times$ 200 mm. In [30], a passive and active stereo vision system was used for reconstructing the surface of the deformed plate. In the system, passive stereo vision is used to detect the surface boundary, while active stereo vision with a projection of structured light is used for 3-D reconstruction. In an experiment with a rectangular plate of size 11.65 $\times$ 7.35 cm, at a working distance of about 40 cm, the measuring error in depth was within 2 mm, and the error in the x- and y-directions was within 1 mm.

Shiny surface with strong reflective nature is still a challenge to optical-based instrumentations including structured light means. Sinusoidal structure in the projected pattern [9]–[11], [25], [26] is destroyed in the image data owing to the strong reflections, and the projected lines are also usually flooded and undistinguishable in the captured image [27]. To improve the structured light pattern's antireflection capability, a strip-edge-based coding strategy is proposed in this paper. Compared with the image-intensity-based sinusoidal pattern and the thin-line-based line-shifting pattern, the strips can be better preserved in the image data in the presence of surface reflections, and that makes the coding procedure more robust. To remove the periodic ambiguity within strip patterns, traditional Gray code patterns are brought in. To determine the strip edges more precisely, both the positive and negative patterns are used. In particular, an improved zero-crossing edge detector is proposed for strip-edge localization in subpixel accuracy.

III. Strip-Edge-Based Structured Light Pattern Design and Strip-Edge Detection

The major processes involved in the devised system are thus the following. In the structured light pattern, a unique codeword is assigned to each strip-edge point, which is a combination of a local strip-edge code value and a global Gray code value. The illuminated object surface is then imaged, and the strip edges in the image data are precisely located. Correspondences between the illuminated pattern and the image plane can be established, and spatial depth at the strip-edge points can be determined.

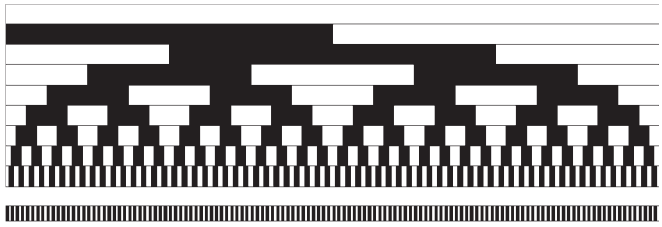

Fig. 2. Coding strategy of Gray code combined with strip shifting pattern. *Top*: Series of Gray code patterns (with $n = 9$) is used to construct 256 subregions each with a unique codeword. *Bottom*: Strip pattern of width 4 pixels is shifted three times to encode positions within each subregion. Strip edges of the shifting pattern will be detected and encoded in finer accuracy.

A. Strip-Edge-Based Coding Strategy

Compared with the raw image intensities and thin image lines that are vulnerable to the reflective nature of shiny surfaces, edges of binary strips in the illuminated pattern are more localizable and better preserved in the image data despite the specular nature of the object surfaces. Higher localizability of the edges comes with more accurate reconstruction and higher robustness of the measurement system.

In the implementation, a series of $(n + 1)$ Gray code patterns is first projected in order to divide the target surface into 2^n subregions (it is not 2^{n+1} regions because the all-zero codeword is not distinguishable in the image data and generally not used), each with a unique n-b-long Gray codeword. Suppose that each of such subregions is m pixel wide on the projector's pattern generation plane. Then, a strip pattern in half of the finest strip width of the Gray code sequence is shifted $m - 1$ times, in steps of 1 pixel, each with a separate image capture by the camera, to encode each subregion with additional bits.

Such a periodic pattern, by itself, has a periodic ambiguity of m pixels (i.e., the width of the strip pattern on the projector's pattern generation plane) in distinguishing different points of the target surface. However, by combining the two codewords together, one from the Gray code and the other from the strip pattern, the m subdivisions can be introduced to each of the 2^n subregions to achieve finer 3-D reconstruction. The procedure can be expressed as

$$\begin{aligned} P &= G + S \\ G &\in \{0, 1, 2, \ldots, (2^n - 1)\} \\ S &\in \{0, 1, 2, \ldots, (m - 1)\} \end{aligned} \tag{1}$$

where S is the local codeword generated by the strip pattern, G is the global Gray codeword used to remove periodic ambiguity among strip patterns, and P is the final unique codeword.

For a pattern generation plane of 1024-pixel width in the projector, Gray code of 9-b length (i.e., $n = 9$) can separate it into 256 subregions. Then, a strip pattern of width 4 pixels is shifted three times in step length of 1 pixel as illustrated by Fig. 2. Upon the shifting, each column of the projector's

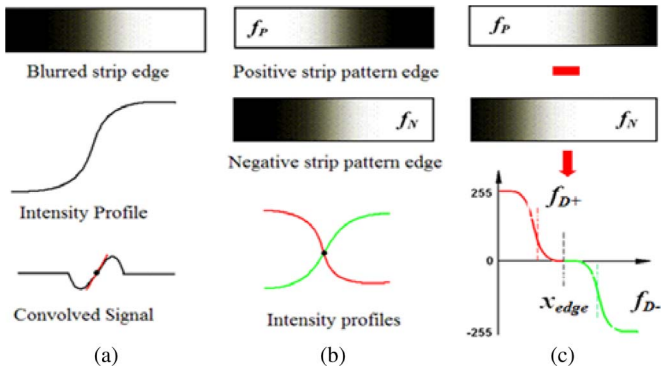

Fig. 3. (a) Zero-crossing edge detector. (b) Without surface reflection, strip-edge position can be determined as the intersection of the positive and negative patterns. (c) Proposed strip-edge detection method in the presence of surface reflection.

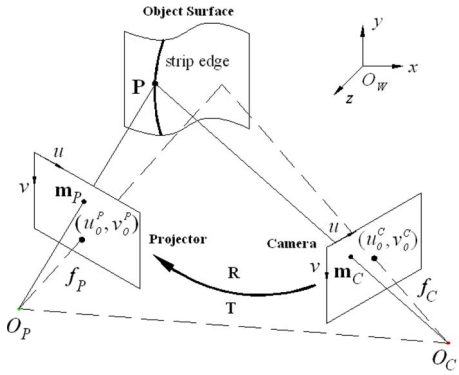

Fig. 4. Geometry between the camera, projector, and world coordinate frames. With the geometry calibrated, depth value of any surface point P can be calculated from the two corresponding points: (u^c, v^c) and (u^p, v^p) in the camera and projector via triangulation.

pixels will be attached with a unique codeword ranging from 0 to 1024.

B. Strip-Edge Detection in Subpixel Accuracy

Strip-edge detection is a crucial step in the system. It affects the final measurement accuracy directly. In previous work, zero crossing of the image intensity is a widely used way of detecting edge location in subpixel accuracy [31]. However, it is sensitive to image noise, and the performance could be seriously affected by surface reflection and noise. In this paper, an alternative method is introduced by projecting both positive and negative patterns to enhance robustness and accuracy.

Subject to the optical limitations (modulation transfer function, depth of field, etc.), the projected strip edges are usually blurred in the captured image as shown in Fig. 3(a). Without considering surface reflection, strip edges can be determined as the intersection lines of the positive strip f_P and the negative strip f_N as shown in Fig. 3(b). Yet, on shiny surface, saturation regions often arise due to strong reflectance. That makes the intersection lines of f_P and f_N unrecognizable. The direct use of zero-crossing edge detector is thus inapplicable. To localize the strip-edge position x_{edge} for shiny surface, an improved zero-crossing approach is proposed.

Suppose that f_D represents the difference image of f_P and f_N as

$$f_D = f_P - f_N. \tag{2}$$

We divide f_D into two segments of f_{D+} and f_{D-} which refer to $f_D > 0$ and $f_D < 0$, respectively, as shown in Fig. 3(c). Zero-crossing positions of f_{D+} and f_{D-} are represented by $x_{\{\nabla^2 f_{D+}=0\}}$ and $x_{\{\nabla^2 f_{D-}=0\}}$, respectively. Then, the strip-edge position x_{edge} in subpixel accuracy can be obtained as

$$x_{\text{edge}} = \left(x_{\{\nabla^2 f_{D+}=0\}} + x_{\{\nabla^2 f_{D-}=0\}}\right)/2. \tag{3}$$

C. System Calibration and 3-D Depth Calculation

The geometry between the camera, projector, and world coordinate frames is illustrated in Fig. 4. Our system uses the perspective model for both the camera and projector [32]. The model can be expressed by the following equation:

$$\begin{bmatrix} \mathbf{m}_{C/P} \\ 1 \end{bmatrix} \cong \underbrace{\begin{bmatrix} \alpha_u^{C/P} & \gamma^{C/P} & u_0^{C/P} \\ 0 & \alpha_v^{C/P} & v_0^{C/P} \\ 0 & 0 & 1 \end{bmatrix}}_{\mathbf{A}_{C/P}} \begin{bmatrix} & & 0 \\ & \mathbf{I}_3 & 0 \\ & & 0 \end{bmatrix} \begin{bmatrix} \mathbf{M}_{C/P} \\ 1 \end{bmatrix} \tag{4}$$

where the subscript C/P refers to whether it is the camera's or the projector's measurement parameters and $\mathbf{m}$ and $\mathbf{M}$ indicate whether it is a 2-D position within the particular sensor (camera or projector) or a 3-D position with respect to the world reference frame. Intrinsic parameters $\alpha_u^C, \alpha_v^C, \gamma^C, u_0^C, v_0^C$ or $\alpha_u^P, \alpha_v^P, \gamma^P, u_0^P, v_0^P$ are collectively expressed as 3×3 matrix $\mathbf{A}_C$ or $\mathbf{A}_P$, where α indicates the scale factors in the u- and v-axes of the sensor array, γ refers to the skew of the sensor axes, and u_0 and v_0 represent the principal point of the sensor plane [32].

The 3-D position $\mathbf{M}_W$ of any space point P, measured against the world coordinate frame, is related to the image position $\mathbf{m}_C$ or $\mathbf{m}_P$ by the following equation:

$$\begin{bmatrix} \mathbf{M}_{C/P} \\ 1 \end{bmatrix} = \underbrace{\begin{bmatrix} \mathbf{R}_{C/P} & \mathbf{T}_{C/P} \\ 0 & 1 \end{bmatrix}}_{\mathbf{E}_{C/P}} \begin{bmatrix} \mathbf{M}_W \\ 1 \end{bmatrix} \tag{5}$$

where $\mathbf{R}$ and $\mathbf{T}$ indicate the rotation and transition matrix between the camera and projector reference frames, respectively. There are six extrinsic parameters $((\mathbf{R}_C, \mathbf{T}_C)$ or $(\mathbf{R}_P, \mathbf{T}_P)$, collectively expressed as 4×4 matrix $\mathbf{E}_C$ or $\mathbf{E}_P)$ for the camera and projector, respectively. With respect to the same world coordinate system, extrinsic parameters $\mathbf{E}_C$ and $\mathbf{E}_P$ of the camera and projector can be defined, and they are related by matrix $\mathbf{E}$—the relative transformation matrix between the projector and camera.

With the aforementioned notations, calibration of our system is about determining the intrinsic parameters $\mathbf{A}_{C/P}$ of the

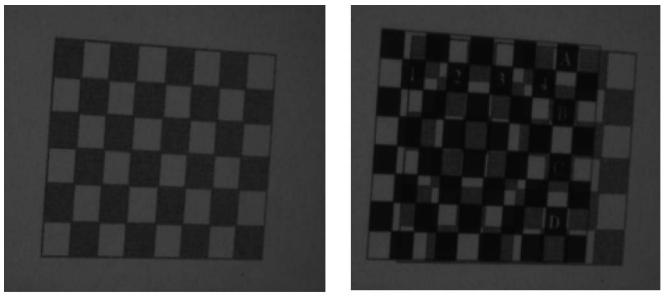

(a) (b)

Fig. 5. System calibration. (a) Printed checker-board pattern is used for calibrating the camera. The checker-board pattern is designed with gray levels of 128 and 255. (b) Separate pattern that is to be projected from the projector to the aforementioned checker board, designed with some markers and in different gray levels (0 and 255), is used for calibrating the projector.

camera and projector, respectively, and the relative transformation matrix $\mathbf{E}$

$$\begin{bmatrix} \mathbf{M}_C \\ 1 \end{bmatrix} \cong \underbrace{\begin{bmatrix} \mathbf{R} & \mathbf{T} \\ 0 & 1 \end{bmatrix}}_{\mathbf{E}} \begin{bmatrix} \mathbf{M}_P \\ 1 \end{bmatrix}. \tag{6}$$

In the calibration procedure, a printed checker-board pattern as shown in Fig. 5(a) is used for calibrating the camera. The pattern is printed with gray levels of 128 and 255, and the pattern forms a calibration board that is to take the place of the object surface in Fig. 4 in the calibration process. Once the calibration board is fixed with respect to the camera and the projector, the camera will first capture one image of the calibration pattern. This image is used for calibrating the camera. Another pattern is then projected by the pico-projector onto the calibration board as shown in Fig. 5(b). The projected pattern is designed with some distinct markers and in gray levels of 0 and 255 so as to make it distinguishable from the original printed one on the calibration board. The camera will then capture the second image of the calibration board. Even though the printed pattern and the projected pattern coexist in the captured image, the markers in the projected pattern can be used to let the grid points be recognized and determined manually. This second image is used for calibrating the projector. By changing the position of the calibration board and repeating the aforementioned procedure 10–15 times, the parameters of the SLS can be calibrated. More details about the calibration process can be found in [33].

The calibration procedure allows the intrinsic parameters $\mathbf{A}_C$ and $\mathbf{A}_P$, the distortion parameters of the camera and projector, and their extrinsic parameters $\mathbf{R}_C, \mathbf{T}_C, \mathbf{R}_P, \mathbf{T}_P$ with respect to a common world coordinate frame to be estimated. With $\mathbf{R}_C, \mathbf{T}_C, \mathbf{R}_P, \mathbf{T}_P$, the relative transformation matrix $\mathbf{E}$ between the camera and projector can be determined from (6).

Suppose that the extracted strip-edge point $\tilde{\mathbf{m}}_c = (x_c, y_c, 1)$ (here, $\tilde{\mathbf{m}}$ represents the projective representation of $\mathbf{m}$) on the camera's image plane and $\tilde{\mathbf{m}}_p = (x_p, y_p, 1)$ on the projector's pattern generation plane are associated with the same scene point. Suppose that the 2-D positions are encoded across the x-dimension. We can relate x_c and x_p by matching the codewords. Using the epipolar constraint [34]

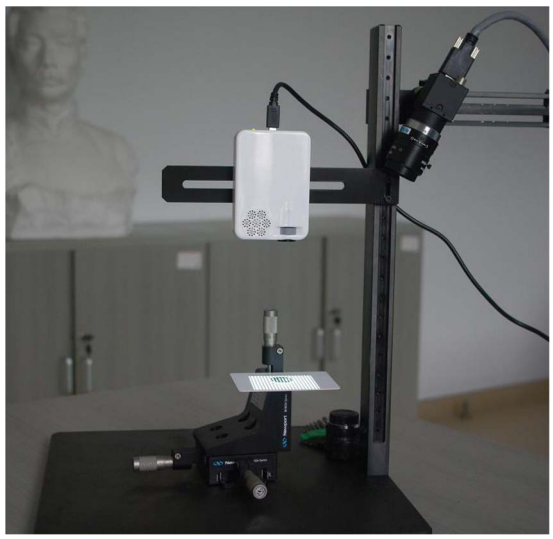

Fig. 6. Experimental setup consists of an off-the-shelf pico-projector and a camera, and the two devices are synchronized.

$$\tilde{\mathbf{m}}_c^T \left(\mathbf{A}_P^{-T} \mathbf{T} \mathbf{A}_C^{-1} \right) \tilde{\mathbf{m}}_p = 0 \tag{7}$$

we can also relate y_c and y_p by solving a linear equation. Once the correspondence problem is solved, the depth z_c of the associated scene point can be determined via traditional triangulation algorithm [8] as

$$z_c = \frac{(\mathbf{R}\tilde{\mathbf{m}}_c \cdot \tilde{\mathbf{m}}_p)(\tilde{\mathbf{m}}_p \cdot \mathbf{T}) - \|\tilde{\mathbf{m}}_p\|^2 (\mathbf{R}\tilde{\mathbf{m}}_c \cdot \mathbf{T})}{\|\mathbf{R}\tilde{\mathbf{m}}_c\|^2 \|\tilde{\mathbf{m}}_p\|^2 - (\mathbf{R}\tilde{\mathbf{m}}_c \cdot \tilde{\mathbf{m}}_p)^2}. \tag{8}$$

IV. Experimental Results

The experimental system is configured with an off-the-shelf pico-projector (3 M liquid crystal on silicon display chip, with a resolution of 640 × 480 pixels, universal serial bus interface, 10 Lux) and a camera (PointGray-Flea2, with a resolution of 1280 × 960 pixels, 30 ft/s), as shown in Fig. 6. The camera is fitted with a Navitar 25-mm lens. All equipment are of merely consumer grade, and the total cost of the apparatus is less than USD 1500. The two devices are configured with a triangulation angle of about 25°–30°. Although larger triangulation angle can boost the measurement accuracy, it also incurs more occlusion and defocus in the image. Since our target object is free-form surface that contains spots of various surface orientations, reflections cannot be much avoided, and image quality cannot be much improved by merely adjusting the projection or imaging angles.

By adjusting the focal planes of both the projector and camera until they overlap, a common projection and imaging zone of about 52 × 39 mm can be achieved at a projection distance of about 150 mm. The system takes about 3 s to complete a full scan. A program written in C++ is used for 3-D calculation. It can process 1.3 million points in less than 1 s on a standard PC platform (Core2 Duo 3.3 GHz, with 4 GB of RAM). Below, we present accuracy evaluation results as well as surface reconstruction of real shiny objects.

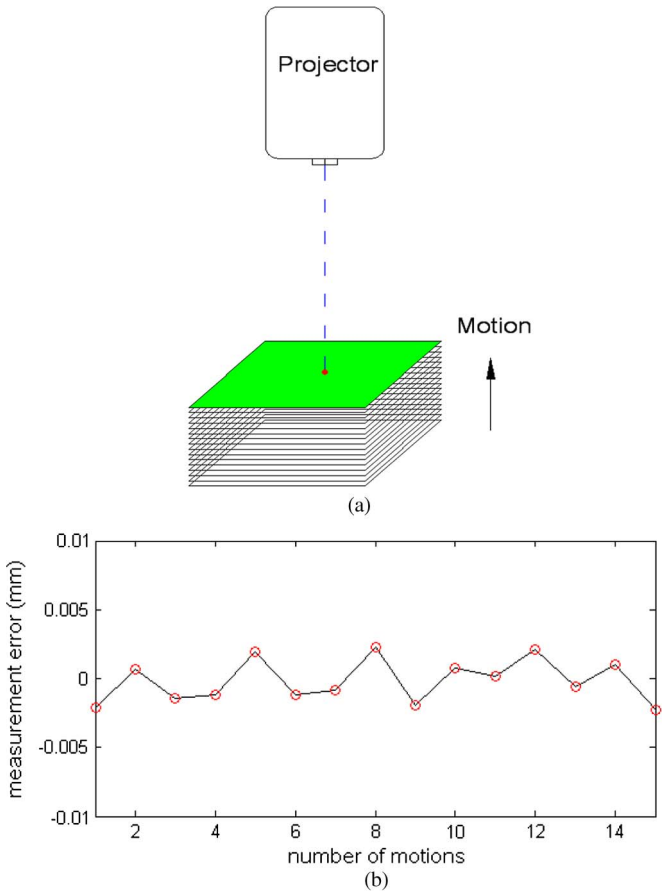

Fig. 7. Reconstruction accuracy evaluation by examining motion of a plane in space. (a) Plane was shifted 16 times toward the projector in steps of 0.1 mm. (b) Error plot of the measured plane displacement at every motion.

TABLE I
PLANE DISPLACEMENT MEASURED AT EVERY MOTION STEP (IN MILLIMETERS)

No.	1	2	3	4	5
Distance	0.1021	0.0993	0.1014	0.1011	0.0980
No.	6	7	8	9	10
Distance	0.1012	0.1008	0.0978	0.1020	0.0992
No.	11	12	13	14	15
Distance	0.0998	0.0979	0.1006	0.0990	0.1022

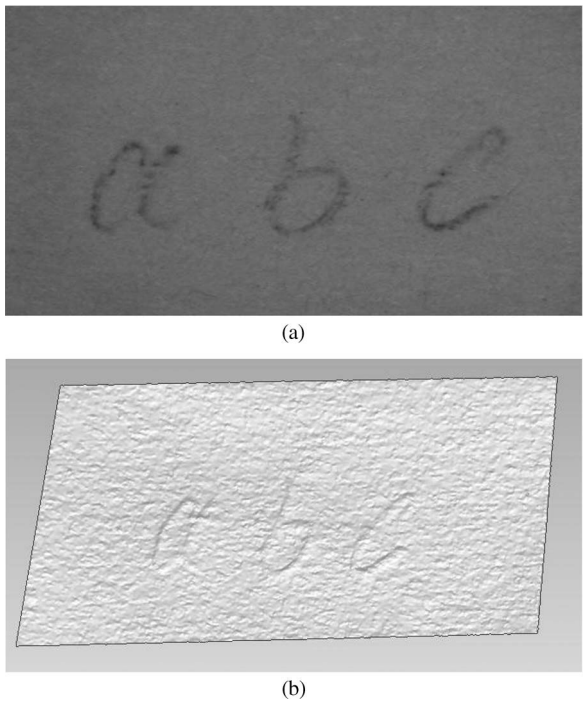

Fig. 8. Three-dimensional reconstruction of a print paper with handwriting. (a) Piece of print paper with some handwritings. (b) Three-dimensional scanning result can discover the erased handwritings as well as the unevenness of the paper surface.

A. *Evaluation of Measurement Accuracy*

In this experiment, the known motion of a plane is used to evaluate the measurement accuracy in depth. A linear stage (Newport M-460A series) with a motion accuracy of 1 μm was used to move an external plane, as shown in Fig. 7(a), in a head-on orientation toward the projector. The plane was shifted 15 times toward the projector in steps of 0.1 mm. After each motion, the described system was used to reconstruct the plane. Altogether, there were 16 planes reconstructed.

As the scanned area of the plane changed slightly over the motion and so did the set of feature points that were reconstructed on the plane, point to point distance calculation at every step of the motion was not possible. Instead, we determined how far the center of the plane traveled in each motion step and compared that with the commanded motion step of the linear stage as an evaluation of how accurately depth was measured by the system. Notice that the inspected plane was not necessarily positioned perfectly orthogonal to the projector's optical axis and the motion was not necessarily perfectly parallel to the projector's optical axis either. These uncertainties could give rise to discrepancies between the measured distance and the commanded motion step, even if the measurement was perfect. Our system's measurement showed that the orientation of the inspected plane was [0.027, 0.055, 0.998] (a unit normal vector) with respect to the projector's coordinate frame, i.e., almost orthogonal to the projector's optical axis but not perfectly so.

The motion steps measured are listed in Table I. The differences between the measurements and the commanded motion steps are plotted in Fig. 7(b). The result shows an absolute mean error of 1.4 μm (and a maximum error of 2.2 μm). Notice that the mean error was very close to the linear stage's resolution, indicating that depth was measured in an accuracy approaching what cannot be measured by the utilities used.

To demonstrate measurement accuracy more intuitively, another experiment was conducted on a print paper with handwritings on it, which is shown in Fig. 8(a). The characters "a, b, c" were handwritten with pencil softly on a sheet of paper and then erased by a rubber. The paper was then scanned by the proposed system for 3-D reconstruction of the handwriting tracks. From the reconstruction result shown in Fig. 8(b), which is about a depth map not an intensity map, it can be observed that the 3-D tracks of the handwriting could be reconstructed to readability by plain eyes. The slight roughness of the paper surface was also made visible in the depth map.

(a) (b)

Fig. 9. Two new shiny coins of different appearances and material that were used in surface reconstruction experimentation.

B. Three-Dimensional Reconstruction of Shiny Coins

To evaluate the system's performance on shiny surface, some shiny coins were tested with, one silvery and the other bronze-like, which are shown in Fig. 9(a) and (b). A sample image of one of the coins, captured under one of the strip pattern projections, is displayed in Fig. 10(a). To restrain the effect of strong reflectance, the aperture of the lens was set to F22. It can be observed that the images were rather dark and of low contrast. In addition, even with so small an aperture, there were still intensity-saturated regions in the image data, caused by the high reflectivity of the coin surface.

The strip-edge detection results are as shown in Fig. 10(b). By the proposed edge detection method, strip edges in dark and intensity-saturated regions could still be extracted largely successfully. The coding map (i.e., an image that shows gray level related to the codeword not appearance brightness of each image position) under coding from the strip patterns alone is shown in Fig. 10(c). The periodic appearance of the same gray level in the coding map shows that periodic ambiguity is present in the codeword. By introducing Gray code patterns, the periodic ambiguity can be removed, and the image points on strip edges can be encoded uniquely, as shown in the associated coding map presented in Fig. 10(d).

The reconstructed surfaces, in their raw form without any smoothing or interpolation introduced, are shown in Fig. 11(a) and (b). It can be observed that even surface features in the dark and intensity-saturated regions could still be recovered with details.

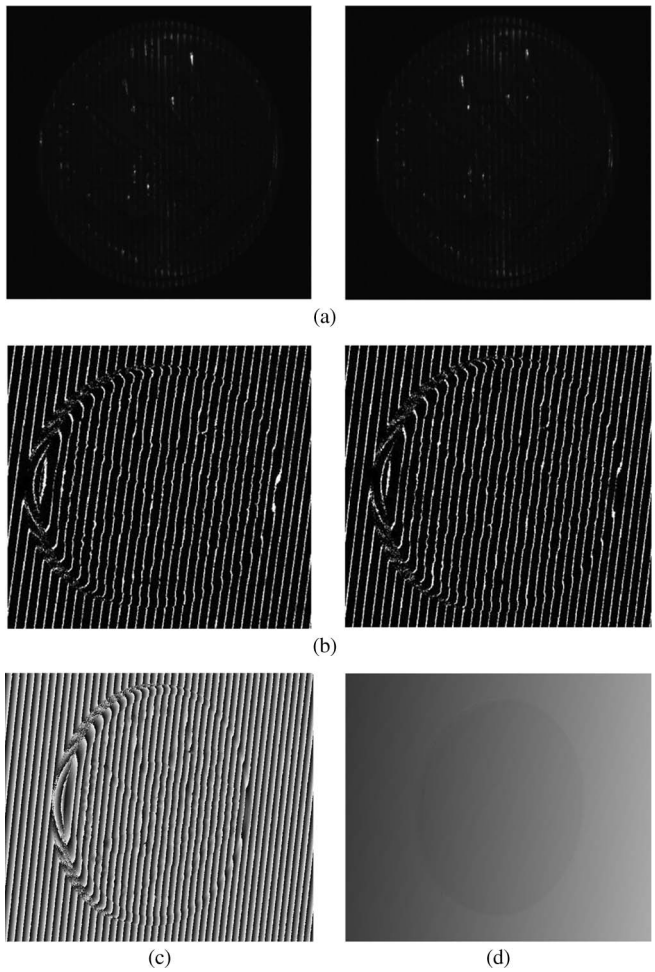

(a) (b) (c) (d)

Fig. 10. (a) Image of one coin under one of the strip pattern projections. (b) Samples of strip-edge detection result. (c) Coding map from the strip patterns alone, which contains periodic ambiguity. (d) Coding map from the strip patterns plus the Gray code patterns, which has no periodic ambiguity.

C. Comparison and Discussion

Without changing the configuration of the experimental setup, a sinusoidal phase-shifting [25] pattern and a line-shifting [27] pattern as shown in Fig. 1 were also implemented for result comparison and evaluation. The sinusoidal phase-shifting pattern is set to have a period of 32 pixels and shifts of 1/4 period each time. In this way, for each given pixel (x, y) of the captured image, four intensity values are obtained: I_1, I_2, I_3, I_4. The phase value $\phi(x, y)$ at the pixel can be determined as

$$\phi(x,y) = \tan^{-1}\left[\frac{I_4(x,y) - I_2(x,y)}{I_1(x,y) - I_3(x,y)}\right].$$

(a) (b)

Fig. 11. Three-dimensional reconstruction results of the coins shown in Fig. 10(a) and (b). Local areas of the reconstructed surfaces are enlarged for close observation.

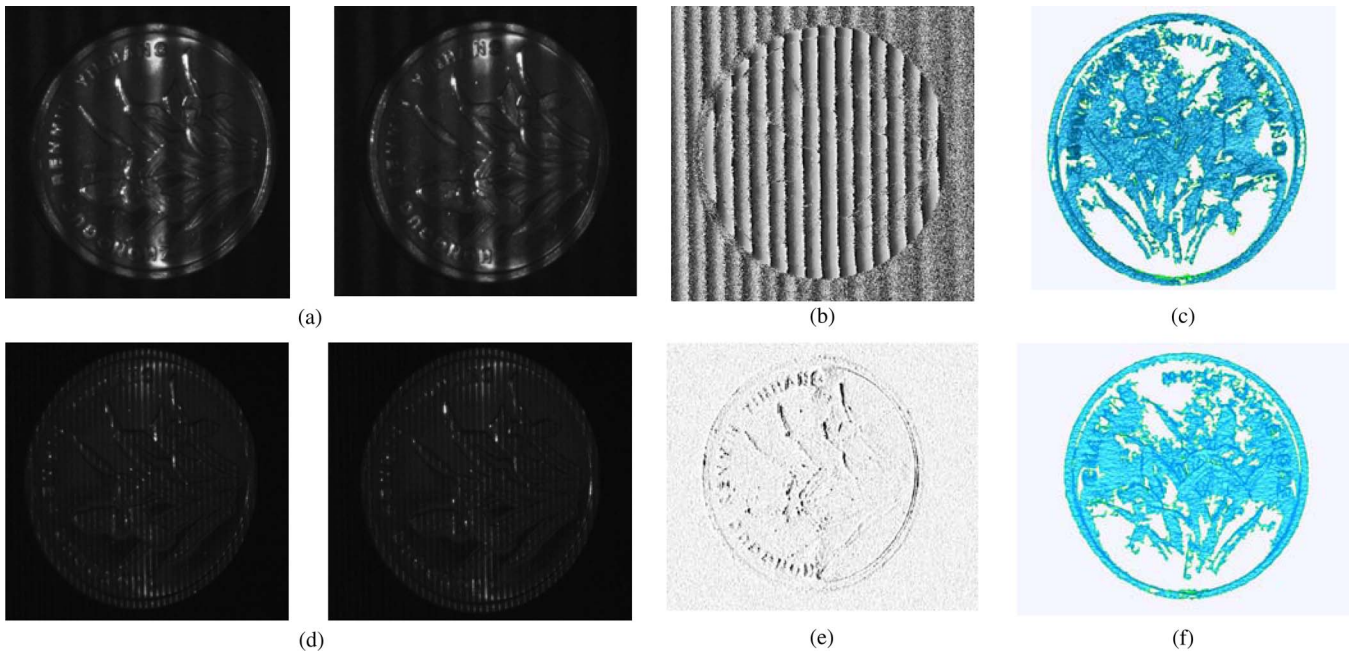

Fig. 12. Results by traditional phase-shifting and line-shifting methods. (a) and (d) Images of one coin under sinusoidal phase-shifting and line-shifting pattern projections. (b) and (e) Coding maps from the phase-shifting and line-shifting patterns alone, which contain periodic ambiguity. (c) and (f) Surface reconstruction results by the phase-shifting and line-shifting methods.

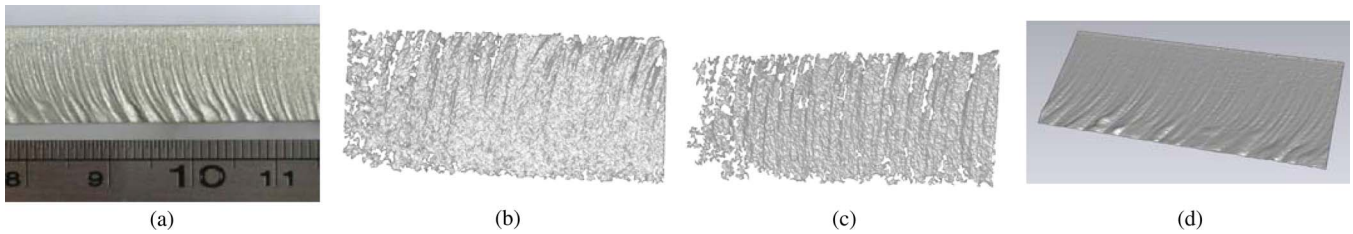

Fig. 13. Reconstruction results of a cutting surface of a metallic workpiece via different methods. (a) Metallic workpiece used for experiment. (b) Result by the phase-shifting method. (c) Result by the line-shifting methods. (d) Result by the proposed method.

The line pattern is set to have a period of 6 pixels and shifts of one pixel each time. As described in [27], the images with line pattern projections are first convolved by a fourth-order filter

$$g_4(i) = f(i-2) + f(i-1) - f(i+1) - f(i+2).$$

The peak centers of projected lines are estimated by a linear interpolation at positions where a change in sign of $g_4(i)$ is encountered in the convolved images [27]. The same Gray code strategy is adopted to remove the periodic ambiguity among sinusoidal and line patterns.

With the aforementioned coding schemes, for the sinusoidal pattern, each image point can be encoded uniquely along the x-direction, and the unique codeword is combined with the local phase value $\phi(x, y)$ and the global Gray code value. For the line pattern, each center point of the line pattern can be encoded uniquely along the x-direction, and the codeword is combined with the local line index value and the global Gray code value. In the 3-D reconstruction stage, the same procedure as described in Section III-C is performed for all the compared algorithms.

From Fig. 12(a) and (d), we can see that the image intensities in both the sinusoidal and line patterns suffered from substantial distortion that was due to the specular nature of the coin surface. That makes the coding maps noisy and unreliable as shown in Fig. 12(b) and (e). As a result, the quality of 3-D reconstruction was greatly compromised.

Fig. 13 shows an experiment with a metallic workpiece. A cutting surface of the metallic workpiece is reconstructed by the phase-shifting, line-shifting, and proposed patterns, respectively. Reconstruction results are as shown in Fig. 13.

Fig. 14 shows an experiment with a ball grid array (BGA) sample. Bumps on the BGA chip are reconstructed by the phase-shifting, line-shifting, and proposed methods. Reconstruction results are as shown in Fig. 14(b)–(d), respectively.

With the aforementioned comparisons, we have demonstrated the advantages of the proposed algorithms. However, if the saturation regions in the image are too large to be included in a single strip, there will be no information constructible in these areas. Visual measurement of mirrorlike free-form shiny surfaces remains a challenging issue.

D. Measurement Accuracy With Shinny Surface

To evaluate the measurement accuracy of shiny surface, a separate experiment was conducted on the same coin that had

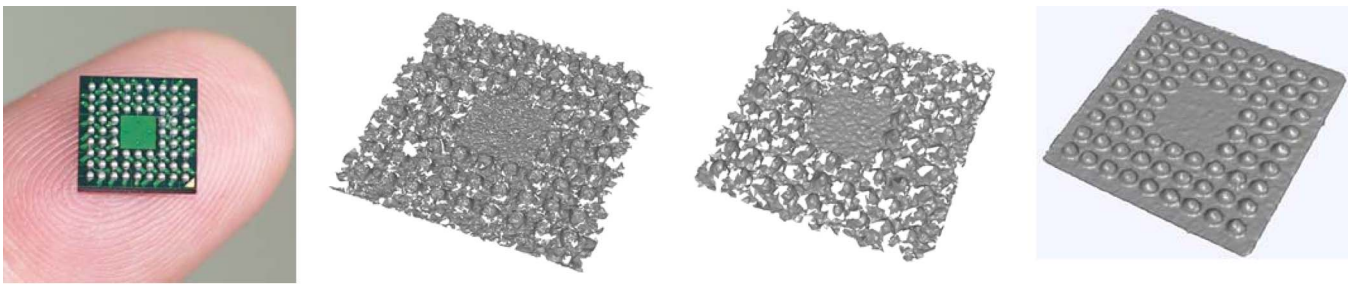

(a) (b) (c) (d)

Fig. 14. Reconstruction results of a BGA sample via different methods. (a) BGA sample used for experiment. (b) Result by the phase-shifting method. (c) Result by the line-shifting methods. (d) Result by the proposed method.

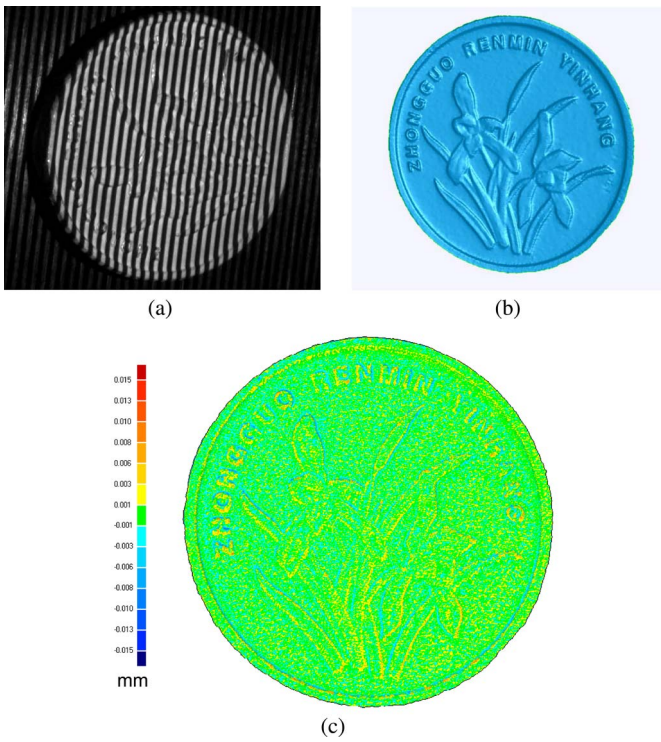

(a) (b) (c)

Fig. 15. Reconstruction of coin surface with coating process for comparison. (a) Coated coin surface under strip pattern illumination. (b) Three-dimensional reconstruction result by the proposed method. (c) Deviation map between the reconstructed coin surfaces with and without coating processing.

undergone a coating process to remove the coin's specularity. As can be observed from Fig. 15(a), the projected strip pattern appeared much sharper because of the great reduction in reflections. Fig. 15(b) shows the reconstructed 3-D model via the proposed method. This reconstruction was taken as the "ground truth" for result evaluation (the tiny thickness and unevenness of the coating material were ignored). To evaluate the deviation between such a reference and the reconstruction result for the original shiny surface (shown in Fig. 11) quantitatively, the two 3-D models are compared in Geomagic which is a widely used business software for point cloud processing. The deviation map is plotted in Fig. 15(c), which shows an absolute mean deviation of 5 μm with a standard deviation of only 7 μm. It can be observed that obvious deviations appeared mainly in the areas with sharp edges and angles where very strong reflections were encountered.

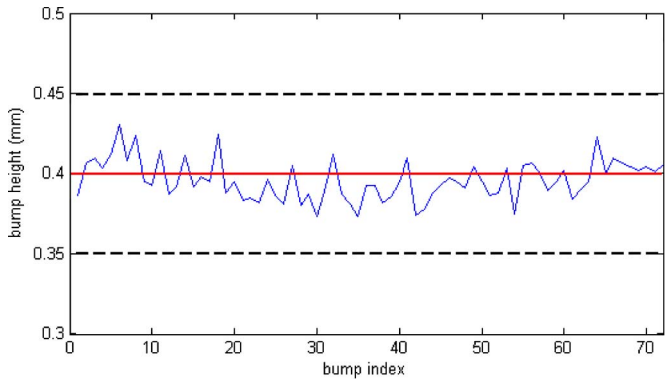

Fig. 16. Height inspection of BGA bumps. The dash lines indicate the allowance range of the bump height.

As shown in Fig. 14, a standard BGA sample with a bump height of 0.4 mm is reconstructed. There are 72 bumps on the BGA chip, and the bump height is a crucial dimension in the packaging procedure. According to the manufacturing requirement, the height deviations of the bumps are required to be controlled to within 0.1 mm. From the reconstruction result by the proposed method as shown in Fig. 14(d), the height of each bump is measured with respect to the BGA baseboard and plotted in Fig. 16. From the result, an average height of 0.396 mm is obtained over all bumps with a standard deviation of only 0.012 mm.

V. Conclusion and Future Work

In this paper, we have described a high-accuracy and robust SLS for 3-D measurement of micro shiny surfaces. A novel strip-edge-based coding strategy is described that enhances the system's robustness against the possible reflective nature of the target surface. To remove the periodic ambiguity, traditional Gray code patterns are adopted. In strip-edge detection, both positive and negative patterns are used. An improved zero-crossing edge detector is also described for detecting strip edges in subpixel accuracy. The system can be built with merely an off-the-shelf pico-projector and a camera and is thus suitable for cost-effective micromeasurement. Extensive experiments on shiny coins, metallic workpiece, and BGA bumps have been used to demonstrate its strong robustness and high measurement accuracy. Previous intensity-based structured light algorithms have also been implemented for result comparison and evaluation.

There is only one camera used in the described system. Subject to the view angle between the camera and projector, some surface areas cannot be imaged and reconstructed due to occlusion. An additional camera mounted on the other side of the projector can supplement more surface information. Future work can address how to align and merge the reconstructed 3-D models from the two different viewpoints so as to enhance the capability of the system in handling the occlusion problem. Owing to the limited response time of the pico-projector that is used, the current system requires 3 s to complete a full scan. In the future, a pico-projection device of faster response time and a high-speed camera are to be adopted for improving the scanning efficiency.

REFERENCES

[1] A. N. Belbachir, M. Hofstätter, M. Litzenberger, and P. Schön, "High-speed embedded-object analysis using a dual-line timed-address-event temporal-contrast vision sensor," *IEEE Trans. Ind. Electron.*, vol. 58, no. 3, pp. 770–783, Mar. 2011.

[2] A. Kumar, "Computer-vision-based fabric defect detection: A survey," *IEEE Trans. Ind. Electron.*, vol. 55, no. 1, pp. 348–363, Jan. 2008.

[3] H. Cho and S. W. Kim, "Mobile robot localization using biased chirp-spread-spectrum ranging," *IEEE Trans. Ind. Electron.*, vol. 57, no. 8, pp. 2826–2835, Aug. 2010.

[4] E. Grosso and M. Tistarelli, "Active dynamic stereo vision," *IEEE Trans. Pattern Anal. Mach. Intell.*, vol. 17, no. 9, pp. 868–879, Sep. 1995.

[5] S. Y. Cho and W. S. Chow, "A neural-learning-based reflectance model for 3-D shape reconstruction," *IEEE Trans. Ind. Electron.*, vol. 47, no. 6, pp. 1346–1350, Dec. 2000.

[6] F. Marino, P. De Ruvo, G. De Ruvo, M. Nitti, and E. Stella, "HiPER 3-D: An omnidirectional sensor for high precision environmental 3-D reconstruction," *IEEE Trans. Ind. Electron.*, vol. 59, no. 1, pp. 579–591, Jan. 2012.

[7] B. Curless, "From range scans to 3D models," *ACM SIGGRAPH Comput. Graph.*, vol. 33, no. 4, pp. 38–41, Nov. 2000.

[8] R. Hartley and P. Sturm, "Triangulation," *Comput. Vis. Image Understanding*, vol. 68, no. 2, pp. 146–157, Nov. 1997.

[9] D. Bergmann, "New approach for automatic surface reconstruction with coded light," in *Proc. SPIE—Remote Sensing Reconstruction Three-Dimensional Objects Scenes*, 1995, vol. 2572, pp. 2–9.

[10] S. Zhang, "Phase unwrapping error reduction framework for a multiple-wavelength phase-shifting algorithm," *Opt. Eng.*, vol. 48, no. 10, p. 105 601, Oct. 2009.

[11] L. Zhang, B. Cudess, and S. M. Seitz, "Rapid shape acquisition using color structured light and multi-pass dynamic programming," in *Proc. Int. Symp. 3D Data Process., Visual., Transm.*, 2002, pp. 24–36.

[12] J. Salvi, S. Fernandez, T. Pribanic, and X. Llado, "A state of the art in structured light patterns for surface profilometry," *Pattern Recognit.*, vol. 43, no. 8, pp. 2666–2680, Aug. 2010.

[13] A. Weckenmann, G. Peggs, and J. Hoffmann, "Probing systems for dimensional micro- and nano-metrology," *Meas. Sci. Technol.*, vol. 17, no. 3, pp. 504–509, Mar. 2006.

[14] S. Jecic and N. Drvar, "The assessment of structured light and laser scanning methods in 3D shape measurements," in *Proc. 4th Int. Congr. Croatian Soc. Mech.*, 2003, pp. 237–244.

[15] M. Yao and B. G. Xu, "Evaluating wrinkles on laminated plastic sheets using 3D laser scanning," *Meas. Sci. Technol.*, vol. 18, no. 12, pp. 3724–3730, Dec. 2007.

[16] G. Saeed and Y. M. Zhang, "Weld pool surface depth measurement using a calibrated camera and structured-light," *Meas. Sci. Technol.*, vol. 18, no. 8, pp. 2570–2578, Aug. 2007.

[17] L. Yao, L. Z. Ma, and D. Wu, "Low cost 3D shape acquisition system using strip shifting pattern," *Digit. Human Model.*, ser. Lecture Notes in Computer Science, vol. 4561, pp. 276–285, 2007.

[18] J. Salvi, J. Pagès, and J. Batlle, "Pattern codification strategies in structured-light systems," *Pattern Recognit.*, vol. 37, no. 4, pp. 827–849, Apr. 2004.

[19] K. C. Wong, P. Y. Niu, and X. He, "Fast acquisition of dense depth data by a new structured-light scheme," *Comput. Vis. Image Understanding*, vol. 98, no. 3, pp. 398–422, Jun. 2005.

[20] Z. Song and R. Chung, "Determining both surface position and orientation in structured-light based sensing," *IEEE Trans. Pattern Anal. Mach. Intell.*, vol. 32, no. 10, pp. 1770–1780, Oct. 2010.

[21] I. C. Albitar, P. Graebling, and C. Doignon, "Robust structured-light coding for 3D reconstruction computer vision," in *Proc. Int. Conf. Comput. Vis.*, 2007, pp. 1–6.

[22] J. Salvi, J. Batlle, and E. Mouaddib, "A robust-coded pattern projection for dynamic 3D scene measurement," *Pattern Recognit. Lett.*, vol. 19, no. 1, pp. 1055–1065, Sep. 1998.

[23] Y. C. Hsieh, "Decoding structured-light patterns for three-dimensional imaging systems," *Pattern Recognit.*, vol. 34, no. 2, pp. 343–349, Feb. 2001.

[24] H. B. Wu, Y. Chen, M. Y. Wu, C. R. Guan, and X. Y. Yu, "3D measurement technology by structured light using stripe-edge-based Gray code," *J. Phys., Conf. Ser.*, vol. 48, no. 48, pp. 537–541, 2006.

[25] F. Sadlo and T. Weyrich, "A practical structured-light acquisition system for point-based geometry and texture," in *Proc. Eur. Symp. Point-Based Graph.*, 2005, pp. 89–98.

[26] H. N. Yen, D. M. Tsai, and S. K. Feng, "Full-field 3D flip-chip solder bumps measurement using DLP-based phase shifting technique," *IEEE Trans. Adv. Packag.*, vol. 31, no. 4, pp. 830–840, Nov. 2008.

[27] J. Gühring, "Dense 3D surface acquisition by structured-light using off-the-shelf components," in *Proc. SPIE*, 2000, vol. 4309, pp. 220–231.

[28] T. Pribanic, H. Dzapo, and J. Salvi, "Efficient and low-cost 3D structured light system based on a modified number-theoretic approach," *EURASIP J. Adv. Signal Process.*, vol. 2010, pp. 474 389-1–474 389-11, 2010.

[29] V. I. Gushov and Y. N. Solodkin, "Automatic processing of fringe patterns in integer interferometers," *Opt. Lasers Eng.*, vol. 14, no. 4/5, pp. 311–324, 1991.

[30] C. Y. Chen and Y. F. Zheng, "Passive and active stereo vision for smooth surface detection of deformed plates," *IEEE Trans. Ind. Electron.*, vol. 42, no. 3, pp. 300–306, Jun. 1995.

[31] D. Ziou and S. Tabbone, "Edge detection techniques: An overview," *Int. J. Pattern Recognit. Image Anal.*, vol. 8, no. 4, pp. 537–559, 1998.

[32] Z. Y. Zhang, "A flexible new technique for camera calibration," *IEEE Trans. Pattern Anal. Mach. Intell.*, vol. 22, no. 11, pp. 1330–1334, Nov. 2000.

[33] Z. Song and R. Chung, "Use of LCD panel for calibrating structured-light-based range sensing system," *IEEE Trans. Instrum. Meas.*, vol. 57, no. 11, pp. 2623–2630, Nov. 2008.

[34] R. Hartley and A. Zisserman, *Multiple View Geometry in Computer Vision*. Cambridge, U.K.: Cambridge Univ. Press, 2004.

Zhan Song received the Ph.D. degree in mechanical and automation engineering from The Chinese University of Hong Kong, Hong Kong, in 2008.

He is currently an Associate Researcher with the Shenzhen Institutes of Advanced Technology, Chinese Academy of Sciences, Shenzhen, China. His research interests include structured light-based sensing and vision-based human–computer interaction.

Ronald Chung (SM'99) received the B.S.E.E. degree from the University of Hong Kong, Hong Kong, and the Ph.D. degree in computer engineering from the University of Southern California, Los Angeles.

He is currently with The Chinese University of Hong Kong, Hong Kong, as the Director of the Computer Vision Laboratory and a Professor in the Department of Mechanical and Automation Engineering. His research interests include computer vision and robotics.

Dr. Chung is a member of MENSA. He was the Chairman of the IEEE Hong Kong Section Joint Chapter on Robotics and Automation Society and Control Systems Society in the years 2001–2003.

Xiao-Ting Zhang received the M.S. degree in mechanical engineering from Harbin Institute of Technology, Harbin, China, in 2009.

She is currently an Assistant Researcher with the Shenzhen Institutes of Advanced Technology, Chinese Academy of Sciences, Shenzhen, China. Her research interests include computer vision and robotics.